Featured in Physics

# Observation of Integer and Fractional Quantum Anomalous Hall Effects in Twisted Bilayer $MoTe_2$

Fan Xu,[1,2] Zheng Sun,[1] Tongtong Jia,[1] Chang Liu,[1] Cheng Xu,[3,4] Chushan Li,[1] Yu Gu,[1] Kenji Watanabe,[5] Takashi Taniguchi,[6] Bingbing Tong,[7] Jinfeng Jia,[1,2,8] Zhiwen Shi,[1,2] Shengwei Jiang,[1,2] Yang Zhang,[3,9,*] Xiaoxue Liu,[1,2,8,†] and Tingxin Li[1,2,8,‡]

[1]*Key Laboratory of Artificial Structures and Quantum Control (Ministry of Education), Shenyang National Laboratory for Materials Science, School of Physics and Astronomy, Shanghai Jiao Tong University, Shanghai 200240, China*
[2]*Tsung-Dao Lee Institute, Shanghai Jiao Tong University, Shanghai 201210, China*
[3]*Department of Physics and Astronomy, University of Tennessee, Knoxville, Tennessee 37996, USA*
[4]*State Key Laboratory of Low Dimensional Quantum Physics and Department of Physics, Tsinghua University, 100084 Beijing, China*
[5]*Research Center for Electronic and Optical Materials, National Institute for Materials Science, 1-1 Namiki, Tsukuba 305-0044, Japan*
[6]*Research Center for Materials Nanoarchitectonics, National Institute for Materials Science, 1-1 Namiki, Tsukuba 305-0044, Japan*
[7]*Beijing National Laboratory for Condensed Matter Physics and Institute of Physics, Chinese Academy of Sciences, Beijing 100190, China*
[8]*Hefei National Laboratory, Hefei 230088, China*
[9]*Min H. Kao Department of Electrical Engineering and Computer Science, University of Tennessee, Knoxville, Tennessee 37996, USA*

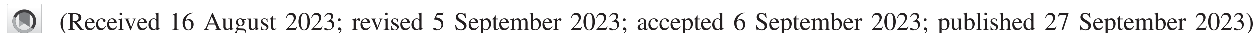

(Received 16 August 2023; revised 5 September 2023; accepted 6 September 2023; published 27 September 2023)

The interplay between strong correlations and topology can lead to the emergence of intriguing quantum states of matter. One well-known example is the fractional quantum Hall effect, where exotic electron fluids with fractionally charged excitations form in partially filled Landau levels. The emergence of topological moiré flat bands provides exciting opportunities to realize the lattice analogs of both the integer and fractional quantum Hall effects without the need for an external magnetic field. These effects are known as the integer and fractional quantum anomalous Hall (IQAH and FQAH) effects. Here, we present direct transport evidence of the existence of both IQAH and FQAH effects in small-angle-twisted bilayer $MoTe_2$. At zero magnetic field, we observe well-quantized Hall resistance of $h/e^2$ around moiré filling factor $\nu = -1$ (corresponding to one hole per moiré unit cell), and nearly quantized Hall resistance of $3h/2e^2$ around $\nu = -2/3$, respectively. Concomitantly, the longitudinal resistance exhibits distinct minima around $\nu = -1$ and $-2/3$. The application of an electric field induces topological quantum phase transition from the IQAH state to a charge transfer insulator at $\nu = -1$, and from the FQAH state to a topologically trivial correlated insulator, further transitioning to a metallic state at $\nu = -2/3$. Our study paves the way for the investigation of fractionally charged excitations and anyonic statistics at zero magnetic field based on semiconductor moiré materials.

DOI: 10.1103/PhysRevX.13.031037 Subject Areas: Condensed Matter Physics

## I. INTRODUCTION

Integer quantum anomalous Hall (IQAH) effects [1–3], characterized by well-quantized Hall resistance of $h/ne^2$ (where $n$ is an integer and $h$ and $e$ denote the Planck's constant and electron charge, respectively) and vanishing longitudinal resistance at zero magnetic field, have already been successfully demonstrated in several material systems [4–7]. In conjunction with strong electron-electron interactions, the partially filled Chern bands can host the fractional quantum anomalous Hall (FQAH) states [8–12],

*yangzhang@utk.edu
†xxliu90@sjtu.edu.cn
‡txli89@sjtu.edu.cn

*Published by the American Physical Society under the terms of the Creative Commons Attribution 4.0 International license. Further distribution of this work must maintain attribution to the author(s) and the published article's title, journal citation, and DOI.*

in analogy to the fractional quantum Hall effects from partially filled Landau levels [13,14]. However, realizing FQAH effect turns out to be considerably more challenging in real materials due to the requirement of nearly uniform Berry curvature distributions within a topological flat band. Chern bands formed in graphene moiré superlattices have been considered [15–21] as a tunable platform to realize FQAH effect. A recent experiment [22] has reported fractional Chern insulator states in twisted bilayer graphene, but only under a 5 T external magnetic field. This external magnetic field is essential for redistributing the Berry curvature inside the topological moiré band to enable the fractional Chern insulator states. On the other hand, semiconductor moiré materials [23,24] offer another promising avenue for engineering topological and strong correlation physics. Experimental studies have demonstrated [7,25] tunable band topology and IQAH effect in near-60-degree-twisted (commonly referred to as AB-stacked) $MoTe_2/WSe_2$ moiré heterostructures. Theoretical works [26–29] also suggest semiconductor moiré systems have the potential to host both IQAH and FQAH effects. Specifically, the low energy physics in small-angle-twisted (commonly referred to as AA-stacked) bilayer $MoTe_2$ and $WSe_2$ is proposed to be described by the Kane-Mele-Hubbard model, and exhibits flat Chern bands at small twist angles. Recently, electrically tunable magnetism has been reported in twisted bilayer $MoTe_2$ ($t$$MoTe_2$) [30]. Moreover, signatures of IQAH and FQAH states have been observed through photoluminescence [31] and optical compressibility measurements [32] in $t$$MoTe_2$, attracting great interest [33–37]. Another experiment [38] reported integer Chern insulators at zero magnetic field in twisted bilayer $WSe_2$ through local compressibility measurements. However, definitive and indisputable evidence of both IQAH and FQAH effects in these systems, namely the quantized Hall conductance, is still lacking.

In this study, we report transport evidence of the existence of both IQAH and FQAH effects in $t$$MoTe_2$. We fabricated AA-stacked $MoTe_2$ bilayer devices with twisted angle of ∼3.7–3.85 deg and conducted systematic transport measurements. The schematic structure of the device is depicted in Fig. 1(a), where the moiré filling factor ($\nu$) and the vertical electric displacement field ($D$) can be independently controlled by the top gate voltage $V_t$ and back gate voltage $V_b$. To achieve Ohmic contacts, the $MoTe_2$ layer is directly touched with few-layer $TaSe_2$ and we employ the global $Si/SiO_2$ gate to induce heavy hole doping in the contact region (see Appendix A for detailed information of device fabrications and transport measurements). At $\nu = -1$, we observe quantized Hall conductance plateau (within certain $\nu$ and $D$ ranges) of $e^2/h$ at zero magnetic field. Similarly, at $\nu = -2/3$, quantized Hall conductance plateau of $2e^2/3h$ has been observed in the zero magnetic field limit, albeit within a narrower range of $\nu$ and $D$ as compared to $\nu = -1$. The longitudinal resistance concomitantly exhibits distinct minima within similar $\nu$ and $D$ ranges. Moreover, both the IQAH and FQAH states can be tuned into topologically trivial states by applied $D$ field.

## II. IQAH EFFECT AT $\nu = -1$ AND FQAH EFFECT AT $\nu = -2/3$

Figures 1(b) and 1(c) present the longitudinal sheet resistance ($\rho_{xx}$) and the Hall resistance ($\rho_{xy}$) of device I, as a function of $\nu$ and $D$ in the zero magnetic field limit. The moiré density ($n_M$) of device I is estimated to be approximately $3.8 \times 10^{12}$ $cm^{-2}$ (see Appendix C), corresponding to a twisted angle about 3.7 deg. At large $D$ values, the $t$$MoTe_2$ experiences a substantial interlayer potential difference, resulting in a layer-polarized state. In this regime, the physics is predominantly governed by a single-band Hubbard model on triangular lattices [39]. Consequently, we observe a series of topologically trivial correlated insulating states at $\nu = -1$, $\nu = -2/3$, $-1/2$, and $-1/3$. These results are qualitatively consistent with previous observations in transition metal dichalcogenide moiré heterostructures with significant band offset [40–47]. Notably, as the $D$ value decreases, substantial $\rho_{xy}$ emerge within the $\nu$ range of $\sim -1.25$ to $\sim -0.5$, particularly near $\nu = -1$ and $\nu = -2/3$, demonstrating spontaneous time reversal symmetry (TRS) breaking in these regions. It is evident that the critical electric field ($D_c$) required to suppress the spontaneously TRS breaking phase gradually decreases with decreasing hole density, which is consist with recent optical studies [30–32]. Additionally, within the region where TRS is spontaneously broken, $R_{xx}$ exhibits minima around $\nu = -1$ and $\nu = -2/3$. These are distinctive attributes of chiral edge transport—a significant indicator of the presence of quantum anomalous Hall effects.

We further investigate the spontaneously TRS breaking states around $\nu = -1$ and $\nu = -2/3$. Figures 2(a) and 2(b) illustrate $\rho_{xy}$ and $\rho_{xx}$, respectively, as a function of out-of-plane magnetic field ($B$) at $\nu = -1$ and $D = -115$ mV/nm [see Supplemental Material Figs. 1(a)–1(c) for other $D$ values [48] ]. A clear magnetic hysteresis loop with coercive field around 30 mT at 30 mK is observed. At zero magnetic field, $\rho_{xy}$ remains quantized at $h/e^2$ ($\pm 1.5\%$) below 2 K. Correspondingly, $\rho_{xx}$ is almost vanishing at low temperatures (<100 Ω below 900 mK), and shows two sharp peaks at the coercive fields. With increasing temperature, the $\rho_{xy}$ at $B = 0$ begins to deviate from its quantized value while, simultaneously, $\rho_{xx}$ at $B = 0$ undergoes rapid growth. The Curie temperature at $\nu = -1$ is determined to be about 10–12 K by the temperature-dependent $\rho_{xy}$ at $B = 0$ [see Supplemental Material Fig. 1(d) [48] ].

We now turn to the $\nu = -2/3$ state. Figures 2(c) and 2(d) show $\rho_{xy}$ and $\rho_{xx}$, respectively, at $\nu = -2/3$ and $D = 5$ mV/nm, as a function of $B$ at temperature ($T$)

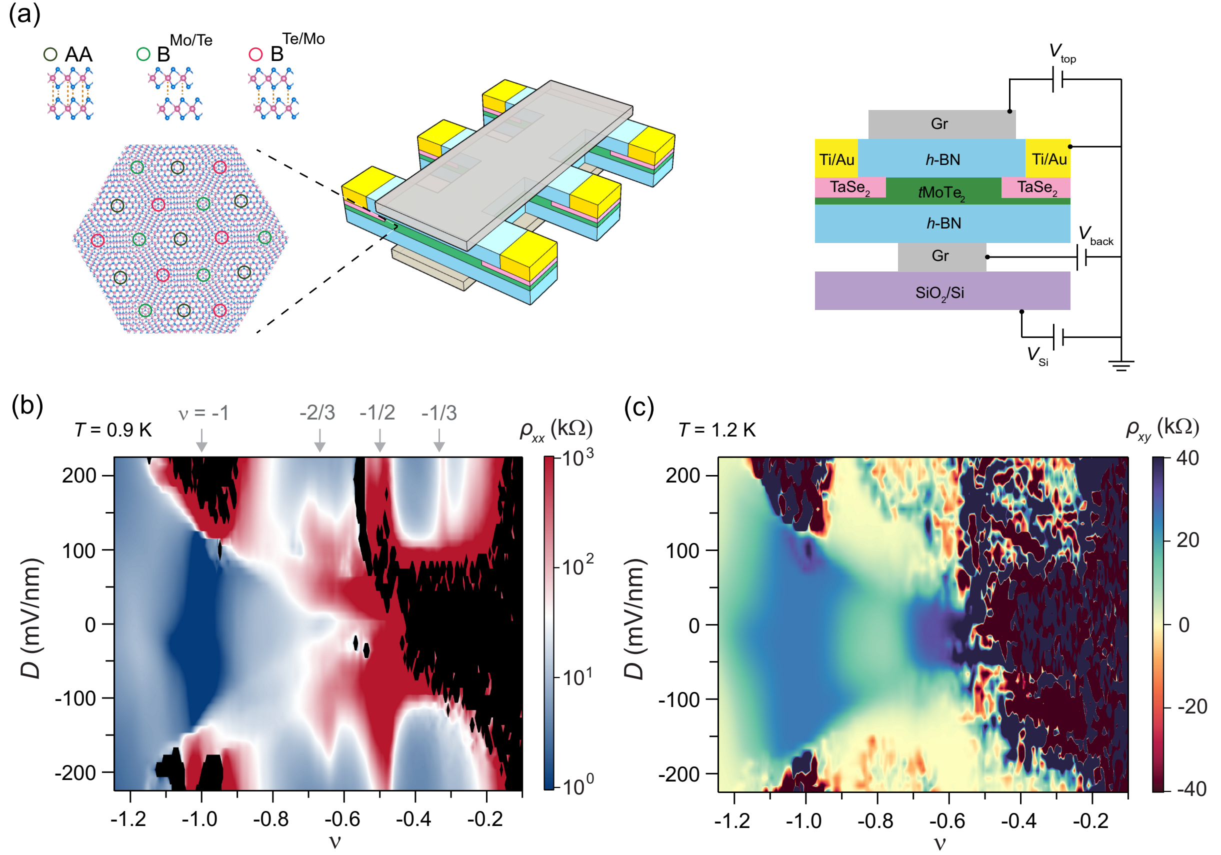


FIG. 1. Phase diagram of AA-stacked $t\mathrm{MoTe_2}$. (a) Left: schematic of the Hall bar device used for transport measurements. Right: side view of the device structure. The carrier density of the Hall bar channel is only controlled by the top gate and the back gate, whereas the carrier density of $\mathrm{TaSe_2/MoTe_2}$ contact regions and Hall bar arms are mainly controlled by the global $\mathrm{Si/SiO_2}$ gate. The inset shows the schematic moiré superlattices of $t\mathrm{MoTe_2}$. High symmetry stackings are highlighted by circles. (b) Longitudinal sheet resistance and (c) Hall resistance as a function of $\nu$ and $D$. $\rho_{xx}$ is measured under zero magnetic field at 900 mK; $\rho_{xy}$ is the antisymmetrized results under an out-of-plane magnetic field of $\pm 0.1$ T at 1.2 K. The arrows mark $\nu = -1$, $-2/3$, $-1/2$, and $-1/3$, where correlated insulating states (topologically trivial) formed at relatively large $D$ field. The black regions are very insulating and experimentally inaccessible.

ranging from 600 mK to 6 K. Below 600 mK, electrical contacts at such low fillings become non-Ohmic in this device (see Appendix A), which disturbs reliable transport measurements. Again, at low temperatures (<1 K), we observe clear magnetic hysteresis with coercive field ~5 mT and nearly $B$ independent $\rho_{xy}$ except at the magnetic switching. At 600 mK, the $\rho_{xy}$ at zero magnetic field is close to a quantized value of $3h/2e^2$. At elevated temperatures, $\rho_{xy}$ starts to deviate from the quantized value, and a Curie temperature of ~4 K is determined from the $T$-dependent $\rho_{xy}$ data. On the other hand, although a distinct local minimum of $\rho_{xx}$ can be observed around $\nu = -2/3$, we notice it remains substantial even at 600 mK, approximately around 20 kΩ at $B = 0$. And the $\rho_{xy}$ quantization around $\nu = -2/3$ is less accurate compared to the $\nu = -1$ state (see Appendix B for $\rho_{xx}$ and $\rho_{xy}$ as a function of $\nu$ at varying temperatures, also longitudinal and Hall resistance measured in different contact configurations).

These observations demonstrate that the state at $\nu = -1$ is an IQAH state with Chern number $|C| = 1$ and the state at $\nu = -2/3$ is a FQAH state with $|C| = 2/3$. The imperfection quantization of $\rho_{xy}$ and non-negligible $\rho_{xx}$ of the $\nu = -2/3$ FQAH state arises presumably from the disorder and inhomogeneity of the sample that leads to remnant dissipation in the bulk. It may also relate to the relatively large contact resistance at $\nu = -2/3$ at low temperatures. The $\nu = -1$ state is more robust because of a much larger gap compared to the $\nu = -2/3$ state. Independently, the Chern number can be deduced from the Streda formula, $n_M(d\nu/dB) = C(e/h)$, which has been commonly used to determine the Chern number of quantum anomalous Hall states or Chern states in moiré systems [5,7,21,22,31,32,38]. We checked the dispersion of $\rho_{xx}$ in $\nu$ and $B$, and extracted the Chern number for the $\nu = -1$ and $\nu = -2/3$ states to be $|C| = 1.05 \pm 0.09$ and $|C| = 0.6 \pm 0.05$, respectively (see Appendix C). The results are reasonably consistent with the observed

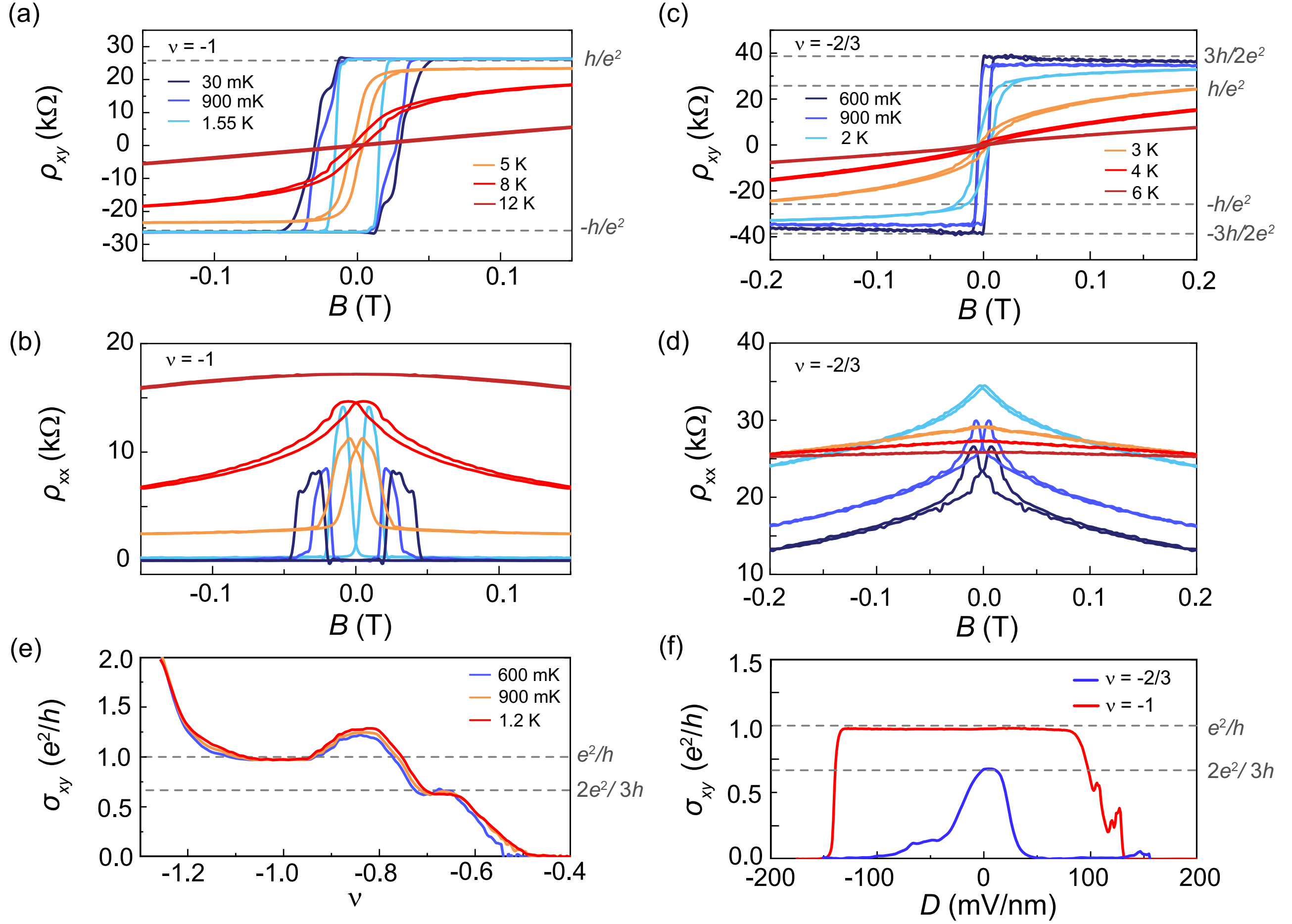


FIG. 2. IQAH effect at $\nu = -1$ and FQAH effect at $\nu = -2/3$. (a),(b) Magnetic-field dependence of $\rho_{xy}$ (a) and $\rho_{xx}$ (b) of the IQAH effect at $\nu = -1$ and $D = -115$ mV/nm at varying temperatures. Quantized $\rho_{xy}$ of $h/e^2$ and vanishing $\rho_{xx}$ are observed below 2 K at zero magnetic field. (c),(d) Magnetic-field dependence of $\rho_{xy}$ (c) and $\rho_{xx}$ (d) of the FQAH effect at $\nu = -2/3$ and $D = 5$ mV/nm at varying temperatures. Nearly quantized $\rho_{xy}$ of $3h/2e^2$ can be observed. (e) Hall conductivity $\sigma_{xy}$ as a function of $\nu$ at $T = 600$ mK, 900 mK, and 1.2 K with $D = 5$ mV/nm. The $\sigma_{xy}$ is obtained using the antisymmetrized $\rho_{xy}$ and symmetrized $\rho_{xx}$ at $B = \pm 0.3$ T. Distinct $\sigma_{xy}$ plateaus can be observed around $\nu = -1$ and $-2/3$, with values closely approaching the quantized values of $e^2/h$ and $2e^2/3h$, respectively. (f) $\sigma_{xy}$ as a function of $D$ measured at 900 mK at $\nu = -1$ and $\nu = -2/3$. The $\sigma_{xy}$ remains at the quantized values within certain $D$ range, then rapidly vanishes as $D$ reaches $D_c$. For $\nu = -1$, $\sigma_{xy}$ is derived from measured $\rho_{xy}$ and $\rho_{xx}$ at $B = 0$ T, and for $\nu = -2/3$, $\sigma_{xy}$ is obtained from antisymmetrized $\rho_{xy}$ and symmetrized $\rho_{xx}$ at $B = \pm 0.3$ T.

quantized Hall resistance, and recent optical studies [31,32]. The difference between the experimental values and the anticipated values ($|C| = 1$ and $2/3$) may also be related to sample inhomogeneities and disorder effects. These results are qualitatively reproduced in another pair of contacts (see Appendixes B and C), and also in another device (Supplemental Material Fig. 2 [48]).

## III. QUANTIZED HALL CONDUCTANCE PLATEAU

We further characterize the Hall conductance $\sigma_{xy}$ against $\nu$ and $D$. Figure 2(e) shows $\sigma_{xy}$ as a function of $\nu$ at $D = 5$ mV/nm, across varying temperatures. We derive $\sigma_{xy}$ using the reciprocal resistance-to-conductance tensor conversion given by $\sigma_{xy} = [\rho_{xy}/(\rho_{xx}^2 + \rho_{xy}^2)]$, where the $\rho_{xy}$ ($\rho_{xx}$) is antisymmetrized (symmetrized) at $B = \pm 0.3$ T (see Appendix B). Remarkably, $\sigma_{xy}$ exhibits quantization plateau at $e^2/h$ ($\pm 2\%$) approximately within the range of $\nu = -1.1$ to $-0.95$, and this quantized range narrows with increasing temperature. Around the $\nu = -2/3$ filling, a narrower $\sigma_{xy}$ plateau is evident, spanning from roughly $\nu = -0.65$ to $-0.7$, where the plateau value closely aligns with $2e^2/3h$ ($\pm 5\%$). Figure 2(f) further displays $\sigma_{xy}$ as a function of $D$ at $\nu = -1$ and $\nu = -2/3$ in the zero magnetic field limit at 900 mK. The $\sigma_{xy}$ remains at the quantized values within a specific range of $D$, until the $D$-field induced topological phase transition takes place. The critical electric field $D_c$ of the topological phase transition is estimated to be about 120 and 15 mV/nm for $\nu = -1$

and $\nu = -2/3$, respectively. These results illustrate that the Hall quantization of $\nu = -1$ and $\nu = -2/3$ is robust against the perturbation of $\nu$ and $D$.

Besides the $\nu = -1$ and $\nu = -2/3$ quantization plateaus, large anomalous Hall effects appear at wide parameter regions, which is consistent with strong ferromagnetism observed from the $\rho_{xy}$ map [Fig. 1(c)]. At $\nu < -1$, we observed an increasing anomalous Hall conductance significantly larger than $e^2/h$, which indicates that the second moiré band has the same Chern number (instead of opposite Chern number) as the first moiré band. The overall trend can be captured by mean field calculation with the projected interaction model (see Appendix D and Supplemental Material Fig. 3 [48]). Here the anomalous Hall metal phases preserve translation symmetry, and is a fully polarized metal governed by strong direct exchange interaction between $B^{Mo/Te}$ and $B^{Te/Mo}$ Wannier orbitals. The larger than $e^2/h$ anomalous Hall conductance between $-1 < \nu < -0.8$ and the evident temperature dependence in Fig. 2(e) imply that there is an additional extrinsic contribution from mobile charge carriers besides the intrinsic mechanism of Berry curvature.

## IV. *D*-FIELD INDUCED TOPOLOGICAL PHASE TRANSITION

Next, we examine the topological phase transitions driven by $D$ field at both $\nu = -1$ and $\nu = -2/3$. Figures 3(a) and 3(b) display $\rho_{xx}$ maps versus $D$ and $T$ at $\nu = -1$ and $\nu = -2/3$, respectively. At $\nu = -1$, the system hosts IQAH effect at $|D| < \sim 120$ mV/nm, where $\rho_{xx}$ decrease rapidly with decreasing $T$ below ∼10 K (close to the Cuire $T$ at $\nu = -1$) due to dissipationless chiral edge transport. Above 10 K, $\rho_{xx}$ exhibits a weaker temperature dependence but still increases with raising $T$ (see Supplemental Material Fig. 4 [48]). This behavior contrasts with the temperature dependence of the IQAH effect in AB-stacked $MoTe_2/WSe_2$ [7], where $\rho_{xx}$ exhibits an insulating behavior above the Cuire $T$. On the other hand, at larger $D$ values, the system transitions into a topologically trivial insulator, resulting in a thermal activation behavior with $\rho_{xx}$ growing rapidly with decreasing $T$.

Regarding the $\nu = -2/3$ states, five distinctive regions can be identified, as illustrated in Figs. 3(b) and 3(d). At $D$ close to zero, the system exhibits FQAH effect, and the application of $D$ field drives the FQAH state to a topologically trivial correlated insulator state. Further increasing $D$ field suppresses the trivial insulating state and finally drives the system into a metallic state. The FQAH state preserves $C_{2y}$ symmetry, and the applied vertical electric field will break the layer symmetry to form a fractional correlated trivial insulator (commonly referred to as generalized Wigner crystal or charge density wave insulator in literatures) with honeycomb lattice polarized at one layer [49]. Since the bandwidth of the first moiré band gets larger with the applied $D$ field (see Supplemental Material Fig. 3

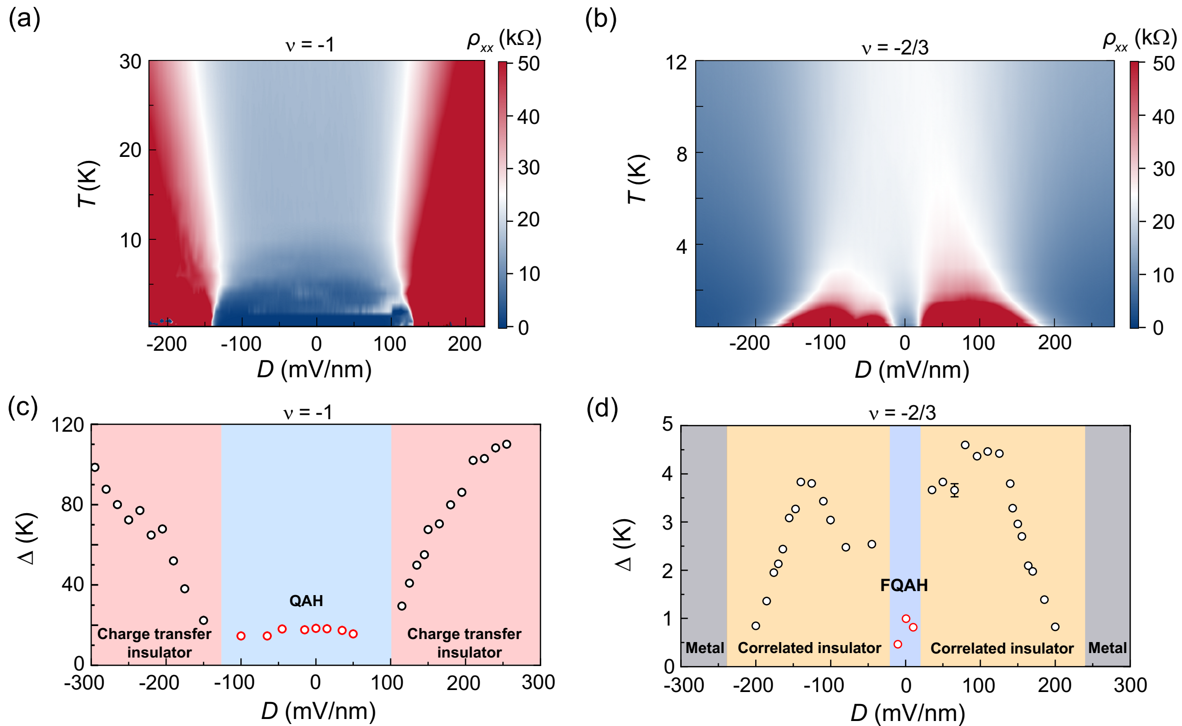


FIG. 3. $D$-field tuned topological phase transitions. (a),(b) $\rho_{xx}$ map as a function of $D$ and $T$ at $\nu = -1$ (a) and $\nu = -2/3$ (b). The $\rho_{xx}$ of $\nu = -1$ is measured at $B = 0$, and the $\rho_{xx}$ of $\nu = -2/3$ is symmetrized at $B = \pm 0.3$ T. (c),(d) Extracted energy gap $\Delta$ (circles) by thermal activation fitting, as a function of $D$, at $\nu = -1$ (c) and $\nu = -2/3$ (d). Distinct phases are differentiated by various colors. The error bars smaller than the size of the circles are not displayed.

[48]), the Wannier functions polarized at a single layer will become more spread out. Therefore, the correlated trivial insulator at $\nu = -2/3$ transits to a metallic state at large $D$ field.

We extract the gap values in both the topologically trivial and nontrivial insulating phases at $\nu = -1$ and $\nu = -2/3$ by thermal activation fitting of $T$-dependent $\rho_{xx}$ (see Supplemental Material Fig. 4 [48]), as shown in Figs. 3(c) and 3(d). Near the boundary of the topological phase transition, the thermal activation fitting becomes invalid due to the coexistence of both bulk and edge transport. For $\nu = -1$, the gap size ($\Delta$) of the IQAH phase at $D = 0$ is around 20 K, and it gradually decreases with the increasing of $D$. In the topologically trivial regime, the gap size rapidly increases, roughly following a linear relationship with increasing $D$. This is fully consistent with the behavior of a charge transfer gap. At $D = 0$, $C_{2y}$ symmetry is preserved and charges are equally distributed at $B^{Mo/Te}$ and $B^{Te/Mo}$ moiré region. At finite $D > 0$, charges transfer from $B^{Mo/Te}$ to $B^{Te/Mo}$, which leads to a gap closing and reopening, forming a charge transfer insulator. The gap size of charge transfer insulator $\Delta_{CTI}$ will be linearly proportional to applied $D$ field, which is confirmed in our Hartree-Fock field simulations (see Supplemental Material Fig. 3). The gap size of $\nu = -2/3$ states is significantly smaller compared to $\nu = -1$, where the maximum $\Delta$ value of the FQAH effect and the fractional correlated trivial insulator is about 1 and 5 K, respectively. Future experimental studies on higher quality samples and theoretical investigations are required to understand the nature of this phase transition and related critical phenomena.

## V. CONCLUSIONS

In conclusion, we have observed both IQAH and FQAH effects in AA-stacked $t\mathrm{MoTe}_2$ through electrical transport measurements. We have further explored the electric-field-driven topological phase transitions involving IQAH, FQAH, and other, topologically trivial correlated states. Future studies are needed to confirm the charge fractionalization and statistic properties of the FQAH state. The present work demonstrates $t\mathrm{MoTe}_2$ as a fertile ground for exploring exotic quantum phenomena arising from electronic correlations and topology.

## ACKNOWLEDGMENTS

We thank Professor Rui-Rui Du, Professor Kin Fai Mak, and Professor Jie Shan for helpful discussions. This work is supported by the National Key R&D Program of China (Grants No. 2022YFA1405400, No. 2022YFA1402702, No. 2022YFA1402404, No. 2021YFA1401400, No. 2021YFA1400100, No. 2021YFA1202902, and No. 2019YFA0308600), the National Natural Science Foundation of China (Grants No. 12174249, No. 92265102, No. 12174250, No. 12141404, and No. 12074244), the Natural Science Foundation of Shanghai (Grant No. 22ZR1430900), the Innovation Program for Quantum Science and Technology (Grants No. 2021ZD0302600 and No. 2021ZD0302500), and the start-up fund of Shanghai Jiao Tong University. X. L. acknowledges the Pujiang Talent Program (Grant No. 22PJ1406700). T. L. and S. J. acknowledge the Shanghai Jiao Tong University 2030 Initiative and Yangyang Development Fund. Y. Z. was supported by the start-up fund at University of Tennessee, Knoxville, and the National Science Foundation Materials Research Science and Engineering Center program through the UT Knoxville Center for Advanced Materials and Manufacturing (Grant No. DMR-2309083). K. W. and T. T. acknowledge support from the JSPS KAKENHI (Grants No. 21H05233 and No. 23H02052) and World Premier International Research Center Initiative (WPI), MEXT, Japan. A portion of this work was carried out at the Synergetic Extreme Condition User Facility (SECUF).

*Note added.*—Recently, we become aware of a recent work that also reports the observation of IQAH and FQAH effects in $t\mathrm{MoTe}_2$ by electrical transport measurements [50].

## APPENDIX A: DEVICE FABRICATIONS

We fabricated the $t\mathrm{MoTe}_2$ devices by standard dry transfer method [51] with polycarbonate stamps. In brief, thin flakes of graphite (3–5 nm), *h*-BN (15–30 nm), $\mathrm{TaSe}_2$ (2–5 nm), and $\mathrm{MoTe}_2$ (monolayer) were mechanically exfoliated onto $\mathrm{Si/SiO}_2$ substrates and identified by optical microscope. The thickness of thin flakes is measured using an atomic-force microscope (AFM). The $\mathrm{MoTe}_2$ monolayer was mechanically cut into two parts by AFM tips. The pickup sequence is top graphite, top *h*-BN, two pieces of $\mathrm{TaSe}_2$, two pieces of monolayer $\mathrm{MoTe}_2$, bottom *h*-BN, and bottom graphite. The twisted angle between the two layers of $\mathrm{MoTe}_2$ monolayer is controlled by a mechanic rotator. Then the entire stack was released onto a $\mathrm{Si/SiO}_2$ substrate. We handled $\mathrm{MoTe}_2$ flakes inside a nitrogen-filled glovebox with oxygen and water levels below one part per million (ppm) to minimize degradation of $\mathrm{MoTe}_2$. Windows were prior opened on the top *h*-BN by *e*-beam lithography (EBL) and reactive ion etching (RIE), then Ti/Au (5 nm/50 nm) electrodes were *e*-beam evaporated in order to contact the $\mathrm{TaSe}_2$ layer. To define the Hall bar geometry of the twisted $\mathrm{MoTe}_2$ channel and eliminate the unavoidable monolayer $\mathrm{MoTe}_2$ region (which could potentially cause an electrical short to the moiré region), we carried out standard EBL and RIE processes. The Hall bar width ($W$) is nominal 1 μm, and the separation between voltage probes ($L$) is nominal 2 μm, as shown in Fig. 4(a). Although the $\mathrm{MoTe}_2$ layer is directly touched with metallic $\mathrm{TaSe}_2$ layer, a large doping is still needed in the contact region to form good Ohmic contact for $\mathrm{MoTe}_2$. Therefore, the global $\mathrm{Si/SiO}_2$ (285 nm)

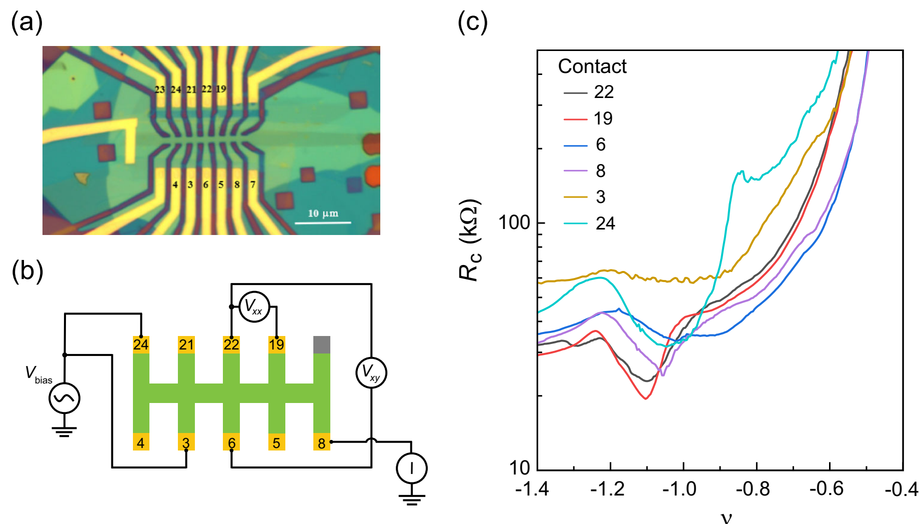


FIG. 4. (a) Optical micrograph of device I. The Hall bar geometry is defined by standard EBL and RIE processes. The scale bar is 10 μm. We found the middle region of the device (between contact 22, 6 and 19, 5) is relatively uniform. (b) Schematic figure of the measurement configuration. For most results presented in the main text, electrode 8 is grounded; electrodes 24 and 3 are used as a source electrode. The longitudinal voltage drop is measured between 22 and 19, and the transverse voltage drop is measured between 22 and 6. (c) Contact resistance versus filling factors at $T = 1.5$ K and $D = 5$ mV/nm. During the measurement of contact resistance, only the specific contact is biased with a 2 mV dc voltage while all other contacts are grounded. The dc current versus filling factors is measured using a source meter.

gate was used to induce heavy hole doping in the contact region during the measurements. The carrier density of the Hall bar channel is only controlled by the top gate and back gate, since the back gate electrodes could screen the electric field from the $Si/SiO_2$ gate. With this device geometry, Ohmic contacts can be achieved irrespective of the applied electric fields. In contrast, the previously used geometry in transition metal dichalcogenide heterostructure devices [7,25,52] can only achieve Ohmic contact for a restricted range of high electric fields. Figure 4(c) displays the measured contact resistance versus filling factors at $T = 1.5$ K and $D = 5$ mV/nm in device I. At lower temperatures, the contact resistance at lower fillings increases more rapidly, going from ~100 kΩ at $\nu = -2/3$ at 1.5 K to ~500 kΩ at $\nu = -2/3$ at 600 mK.

## APPENDIX B: MEASUREMENTS WITH DIFFERENT CONTACT CONFIGURATIONS

Electrical transport measurements were performed in a closed-cycle $^4$He cryostat (Oxford TeslatronPT, base temperature about 1.5 K) with superconducting magnet. Measurements below 1.5 K were performed in a top-loading dilution fridge (Oxford TLM, base temperature about 20 mK) with superconducting magnet. Standard low-frequency (<17 Hz) lock-in (SR830 and SR860) techniques were used to measure the sample resistance. The bias current is limited within 3 nA, especially for measurements below 1.5 K, to avoid sample heating and avoid disturbing the fragile states. Voltage preamplifiers with 100 MΩ impedance were used to measure sample resistance up to several MΩ. Finite longitudinal-transverse coupling occurs in our devices that mixes the longitudinal resistance $R_{xx}$ and Hall resistance $\rho_{xy}$. To correct this effect, we used the standard procedure to symmetrize $[R_{xx}(B) + R_{xx}(-B)]/2$ and antisymmetrize $[\rho_{xy}(B) - \rho_{xy}(-B)]/2$ the measured $R_{xx}$ and

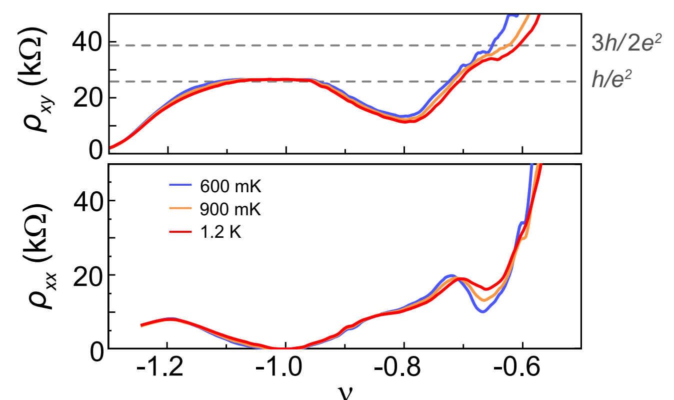


FIG. 5. $\rho_{xy}$ (top) and $\rho_{xx}$ (bottom) as a function of $\nu$ at $T = 600$ mK, 900 mK, and 1.2 K with $D = 5$ mV/nm. The $\rho_{xy}$ ($\rho_{xx}$) is antisymmetrized (symmetrized) at $B = \pm 0.3$ T. $\rho_{xx}$ shows clear dips around $\nu = -1$ and $\nu = -2/3$ due to the chiral edge transport. $\rho_{xy}$ quantized at $h/e^2$ approximately from $\nu = -1.1$ to $-0.95$, and the quantized range becomes narrower with increasing temperature. Around $\nu = -2/3$, a narrower $\rho_{xy}$ plateau can be roughly identified above 900 mK, and the $\rho_{xy}$ value of the plateau is significantly larger than $h/e^2$ but still about 5%–15% smaller than the expected quantized value of $3h/2e^2$. Below 900 mK, the $\rho_{xy}$ plateau around $\nu = -2/3$ becomes indistinguishable, presumably due to the contact issue and sample inhomogeneities.

FIG. 6. (a)–(d) Longitudinal resistance $R_{xx}$ measured with contacts 22, 19, 5, and 6 under different configurations at 600 mK. The specific current bias and voltage measurement configurations are indicated in the insets. (e) Symmetrized $R_{xx}$ as a function of $B$ obtained from (a) and (b) using Onsager reciprocal relations $R_{xx} = (R_{19-22,5-6} + R_{5-6,19-22})/2$. (f) Symmetrized $R_{xx}$ obtained from (c) and (d) using Onsager reciprocal relations $R_{xx} = (R_{22-6,19-5} + R_{19-5,22-6})/2$. (g) Longitudinal sheet resistance $\rho_{xx}$ (symmetrized at $B = \pm 0.3$ T) as a function of $\nu$ measured at 600 mK with another pair of contacts, as illustrated in the inset. (h) Onsager symmetrized $R_{xx} = (R_{19-22,5-6} + R_{5-6,19-22})/2$ as a function of $\nu$ at $B = 0$ T and $T = 600$ mK. Distinct $R_{xx}$ minima can be identified around $\nu = -1$ and $-2/3$ in both (g) and (h).

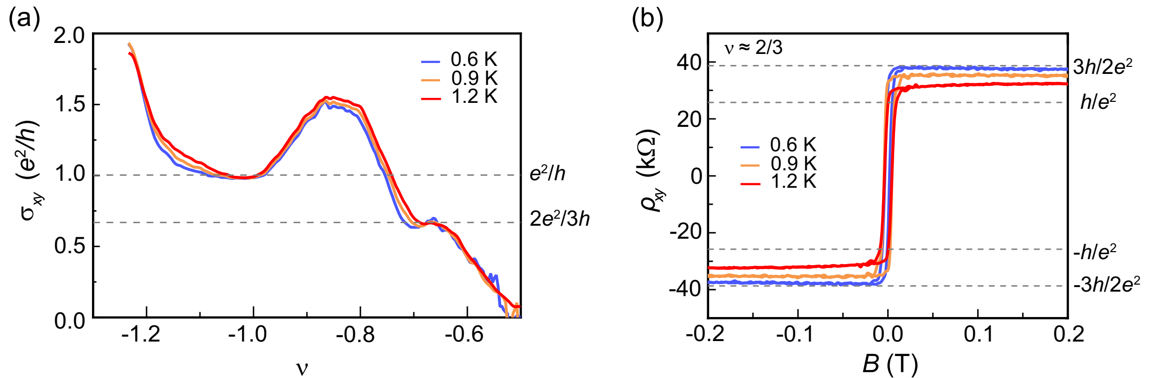


FIG. 7. (a) Hall conductivity $\sigma_{xy}$ as a function of $\nu$ at $T = 600$ mK, 900 mK, and 1.2 K measured from contacts 19–5 with $D = 5$ mV/nm. The $\sigma_{xy}$ is obtained using the antisymmetrized $\rho_{xy}$ and symmetrized $\rho_{xx}$ at $B = \pm 0.3$ T. (b) Magnetic-field dependence of $\rho_{xy}$ at $\nu \approx -2/3$ at varying temperatures measured from contacts 19–5 with $D = 5$ mV/nm. Overall, the results from contacts 19–5 are essentially the same as those from contact 22–6 (shown in Fig. 2).

$\rho_{xy}$ under positive and negative magnetic fields to obtain accurate values of $R_{xx}$ and $\rho_{xy}$, respectively. The longitudinal sheet resistance is derived by $\rho_{xx} = R_{xx}(W/L)$. Figure 5 shows the antisymmetrized $\rho_{xy}$ and symmetrized $\rho_{xx}$ as a function of $\nu$ at varying temperatures.

Alternatively, the Onsager symmetrization method could be performed to disentangle longitudinal and Hall resistance by exchanging the voltage contacts with the current contacts, as illustrated in Fig. 6. The results obtained from magnetic field symmetrization [Figs. 5 and 6(g)] and Onsager symmetrization [Fig. 6(h)] are essentially the same. The Hall quantization results have also been confirmed by measuring Hall resistance with another pair of contacts, as shown in Fig. 7.

## APPENDIX C: DETERMINATION OF MOIRÉ FILLING FACTORS AND STREDA FOMULA FITTING

In dual-gated devices, the carrier density $n = [(c_t V_t + c_b V_b)/e]$ and the effective vertical electric displacement field $D = [(c_t V_t - c_b V_b)/2\varepsilon_0 - D_{\text{built-in}}]$ can be independently controlled by the top gate voltage $V_t$ and back gate voltage $V_b$. Here, $D_{\text{built-in}}$, $\varepsilon_0$, $c_t$, and $c_b$ denote the built-in electric field, vacuum permittivity, top gate capacitance, and back gate capacitance, respectively. The built-in electric field is likely arising from the structure asymmetry. For device I, the $D_{\text{built-in}}$ is about 110 mV/nm, and for device II, the $D_{\text{built-in}}$ is less than 10 mV/nm. The values of $c_t$ and $c_b$ are mainly determined by measuring $h$-BN

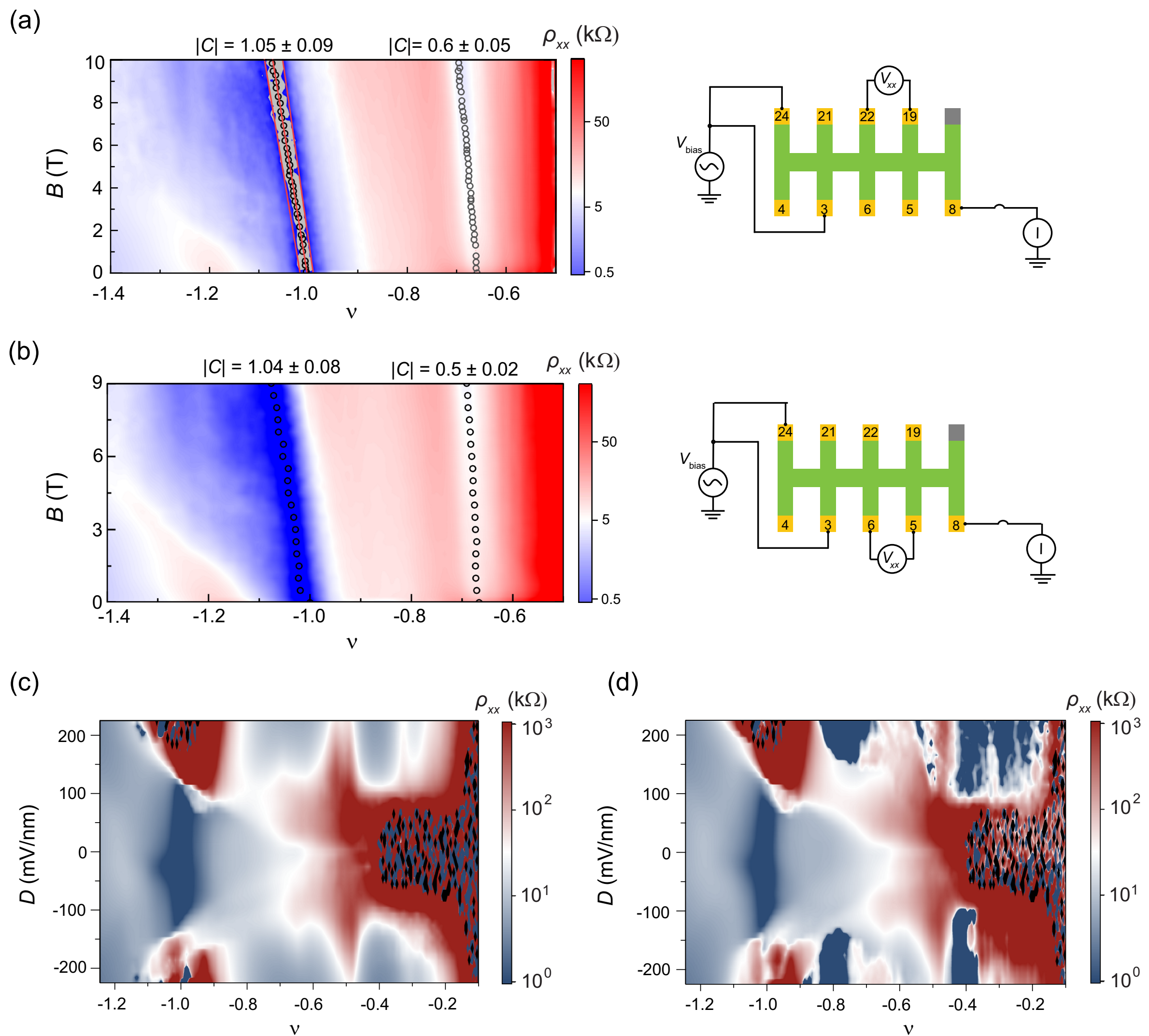


FIG. 8. The $\rho_{xx}$ map as a function of $\nu$ and $B$ at 600 mK with contacts 22–19 (a) and contact 6–5 (b), respectively. Empty circles mark the positions of $\rho_{xx}$ dips around $\nu = -1$ and $-2/3$. Three red lines around $\nu = -1$ in (a) represent possible unbiased fitting lines based on the vanishing $\rho_{xx}$ region, with Chern numbers of 1.13, 1.09, and 0.97, from left to right, respectively. (c),(d) $\rho_{xx}$ (symmetrized at $B = \pm 0.1$ T) map as a function of $\nu$ and $D$ using (c) contacts 22–19 and (d) contacts 6–5 as voltage probes, measured at 1.5 K. The data from contacts 6–5 exhibit lower quality compared to contacts 22–19, which may be attributed to the characteristics of contact 5.

thickness. We convert $n$ to moiré filling factor $\nu$ using the density difference between a series of correlated insulating states with prominent $\rho_{xx}$ peaks.

We performed Streda formula fitting of $\rho_{xx}$ based on the derived moiré filling factor $\nu$ and the moiré density $n_M$, as shown in Fig. 8. The extracted Chern numbers and errors are also displayed in the figures. The deduced Chern numbers show non-negligible deviations from the expected Chern number values. Several factors contribute to this deviation, including disorder effects and sample inhomogeneities. In addition, the broad nature of the $\nu = -1$ feature in $\rho_{xx}$, especially under magnetic fields, makes it challenging to accurately determine the actual position of the $\nu = -1$ gap. As depicted in Fig. 8(a), the gray region represents the region of vanishing $\rho_{xx}$ around $\nu = -1$, where the $\rho_{xx}$ value is smaller than 20 Ω. The three red lines around $\nu = -1$ represent possible unbiased fitting lines based on the gray region, yielding Chern numbers of 1.13, 1.09, and 0.97, from left to right, respectively. We therefore assigned the fitting values and errors by averaging possible fitting results. We note that the $dB/d\nu$ slope measured with contacts 6–5 shows even larger deviation from the expected Chern number of $|C| = 2/3$ for the FQAH state. This might be explained by the nonideal characteristics of contact 5, which is evident from the measured $\rho_{xx}$-$\nu$-$D$ map.

## APPENDIX D: WANNIER PROJECTED TIGHT-BINDING MODEL AND HARTREE-FOCK SIMULATION

The existence of FQAH effect has been discussed with band projected exact diagonalization [34,35]. Here we mainly focus on the understanding of field and filling dependent transition at integer filling and other generic filling factors. We first project the continuum model for the twisted $MoTe_2$ to maximally localized Wannier functions [49], which captures the band dispersion and topological feature of the topmost moiré valence band. The tight-binding model is then constructed as

$$H = t_1 \sum_{\langle i,j \rangle,\alpha} \hat{c}^{\dagger}_{i\alpha} \hat{c}_{j\bar{\alpha}} + t_2 \sum_{\langle\langle i,j \rangle\rangle,\alpha} e^{(-1)^{\alpha} i v_{ij} \phi} \hat{c}^{\dagger}_{i\alpha} \hat{c}_{j\alpha},$$

where $\alpha$ is the index of the sublattice (−1 for $B^{Mo/Te}$ region, +1 for $B^{Te/Mo}$ region), $i$, $j$ is the unit cell index, $t_1$ is the nearest neighbor hopping parameter, $t_2$ and $\phi$ are the amplitude and the phase of second nearest neighbor hopping. This realizes a generalized Kane-Mele model. Since the Wannier functions at $B^{Mo/Te}$ and $B^{Te/Mo}$ are 90% layer polarized, the gating field $D$ will introduce a site potential difference with strength linear in $D$. And the interacting terms in real space are calculated as

$$V = \frac{1}{2} \iint dr dr' \frac{e^2}{\epsilon |\boldsymbol{r} - \boldsymbol{r}'|} \hat{c}^{\dagger}_{\sigma}(\boldsymbol{r}) \hat{c}^{\dagger}_{\sigma'}(\boldsymbol{r}') c_{\sigma'}(\boldsymbol{r}') c_{\sigma}(\boldsymbol{r}).$$

We note that the ferromagnetic exchange interaction term $H_{ex} = \Sigma_{m,n} \Sigma_{\sigma\sigma'} \Sigma_{mn} a^{\dagger}_{m\sigma} a^{\dagger}_{n\sigma'} a_{m\sigma'} a_{n\sigma}$ is crucial for strong ferromagnetism at the wide range of filling factors. To capture the increasing anomalous Hall conductance at $|v| > 1$, we employ the three-band tight-binding model with Chern numbers −1, −1, and 2. With the interacting Hamiltonian in real space, we then perform the Hartree-Fock simulation under parameter space of displacement field and filling factor (which modifies the model parameter) using different supercell configurations. The simulation results are presented in Supplemental Material Fig. 3 [48], which qualitatively capture the filling and displacement field induced transition.


[1] F. D. M. Haldane, *Model for a Quantum Hall Effect without Landau Levels: Condensed-Matter Realization of the "Parity Anomaly,"* Phys. Rev. Lett. **61**, 2015 (1988).

[2] C.-X. Liu, S.-C. Zhang, and X.-L. Qi, *The Quantum Anomalous Hall Effect: Theory and Experiment*, Annu. Rev. Condens. Matter Phys. **7**, 301 (2016).

[3] C.-Z. Chang, C.-X. Liu, and A. H. MacDonald, *Colloquium: Quantum Anomalous Hall Effect*, Rev. Mod. Phys. **95**, 011002 (2023).

[4] C.-Z. Chang *et al.*, *Experimental Observation of the Quantum Anomalous Hall Effect in a Magnetic Topological Insulator*, Science **340**, 167 (2013).

[5] M. Serlin, C. L. Tschirhart, H. Polshyn, Y. Zhang, J. Zhu, K. Watanabe, T. Taniguchi, L. Balents, and A. F. Young, *Intrinsic Quantized Anomalous Hall Effect in a Moiré Heterostructure*, Science **367**, 900 (2020).

[6] Y. Deng, Y. Yu, M. Z. Shi, Z. Guo, Z. Xu, J. Wang, X. H. Chen, and Y. Zhang, *Quantum Anomalous Hall Effect in Intrinsic Magnetic Topological Insulator* $MnBi_2Te_4$, Science **367**, 895 (2020).

[7] T. Li *et al.*, *Quantum Anomalous Hall Effect from Intertwined Moiré Bands*, Nature (London) **600**, 641 (2021).

[8] N. Regnault and B. A. Bernevig, *Fractional Chern Insulator*, Phys. Rev. X **1**, 021014 (2011).

[9] D. N. Sheng, Z.-C. Gu, K. Sun, and L. Sheng, *Fractional Quantum Hall Effect in the Absence of Landau Levels*, Nat. Commun. **2**, 389 (2011).

[10] E. Tang, J.-W. Mei, and X.-G. Wen, *High-Temperature Fractional Quantum Hall States*, Phys. Rev. Lett. **106**, 236802 (2011).

[11] K. Sun, Z. Gu, H. Katsura, and S. Das Sarma, *Nearly Flatbands with Nontrivial Topology*, Phys. Rev. Lett. **106**, 236803 (2011).

[12] T. Neupert, L. Santos, C. Chamon, and C. Mudry, *Fractional Quantum Hall States at Zero Magnetic Field*, Phys. Rev. Lett. **106**, 236804 (2011).

[13] H. L. Stormer, D. C. Tsui, and A. C. Gossard, *The Fractional Quantum Hall Effect*, Rev. Mod. Phys. **71**, S298 (1999).

[14] B. I. Halperin and J. K. Jain, *Fractional Quantum Hall Effects: New Developments* (World Scientific, Singapore, 2020).

[15] C. Repellin and T. Senthil, *Chern Bands of Twisted Bilayer Graphene: Fractional Chern Insulators and Spin Phase Transition*, Phys. Rev. Res. **2**, 023238 (2020).

[16] A. Abouelkomsan, Z. Liu, and E. J. Bergholtz, *Particle-Hole Duality, Emergent Fermi Liquids, and Fractional Chern Insulators in Moiré Flatbands*, Phys. Rev. Lett. **124**, 106803 (2020).

[17] P. J. Ledwith, G. Tarnopolsky, E. Khalaf, and A. Vishwanath, *Fractional Chern Insulator States in Twisted Bilayer Graphene: An Analytical Approach*, Phys. Rev. Res. **2**, 023237 (2020).

[18] Z. Liu, A. Abouelkomsan, and E. J. Bergholtz, *Gate-Tunable Fractional Chern Insulators in Twisted Double Bilayer Graphene*, Phys. Rev. Lett. **126**, 026801 (2021).

[19] P. Wilhelm, T. C. Lang, and A. M. Läuchli, *Interplay of Fractional Chern Insulator and Charge Density Wave Phases in Twisted Bilayer Grapheme*, Phys. Rev. B **103**, 125406 (2021).

[20] D. Parker *et al.*, *Field-Tuned and Zero-Field Fractional Chern Insulators in Magic Angle Graphene*, arXiv:2112.13837.

[21] E. M. Spanton, A. A. Zibrov, H. Zhou, T. Taniguchi, K. Watanabe, M. P. Zaletel, and A. F. Young, *Observation of Fractional Chern Insulators in a van der Waals Heterostructure*, Science **360**, 62 (2018).

[22] Y. Xie *et al.*, *Fractional Chern Insulators in Magic-Angle Twisted Bilayer Grapheme*, Nature (London) **600**, 439 (2021).

[23] D. M. Kennes, M. Claassen, L. Xian, A. Georges, A. J. Millis, J. Hone, C. R. Dean, D. N. Basov, A. N. Pasupathy, and A. Rubio, *Moiré Heterostructures as a Condensed-Matter Quantum Simulator*, Nat. Phys. **17**, 155 (2021).

[24] K. F. Mak and J. Shan, *Semiconductor Moiré Materials*, Nat. Nanotechnol. **17**, 686 (2022).

[25] W. Zhao *et al.*, *Realization of the Haldane Chern Insulator in a Moiré Lattice*, arXiv:2207.02312.

[26] F. Wu, T. Lovorn, E. Tutuc, I. Martin, and A. H. MacDonald, *Topological Insulators in Twisted Transition Metal Dichalcogenide Homobilayers*, Phys. Rev. Lett. **122**, 086402 (2019).

[27] T. Devakul, V. Crépel, Y. Zhang, and L. Fu, *Magic in Twisted Transition Metal Dichalcogenide Bilayers*, Nat. Commun. **12**, 6730 (2021).

[28] H. Li, U. Kumar, K. Sun, and S.-Z. Lin, *Spontaneous Fractional Chern Insulators in Transition Metal Dichalcogenide Moiré Superlattices*, Phys. Rev. Res. **3**, L032070 (2021).

[29] V. Crépel and L. Fu, *Anomalous Hall Metal and Fractional Chern Insulator in Twisted Transition Metal Dichalcogenides*, Phys. Rev. B **107**, L201109 (2023).

[30] E. Anderson, F.-R. Fan, J. Cai, W. Holtzmann, T. Taniguchi, K. Watanabe, D. Xiao, W. Yao, and X. Xu, *Programming Correlated Magnetic States with Gate-Controlled Moiré Geometry*, Science **381**, 325 (2023).

[31] J. Cai *et al.*, *Signatures of Fractional Quantum Anomalous Hall States in Twisted* $MoTe_2$, Nature (London), 10.1038/s41586-023-06289-w (2023).

[32] Y. Zeng *et al.*, *Thermodynamic Evidence of Fractional Chern Insulator in Moiré* $MoTe_2$, Nature (London), 10.1038/s41586-023-06452-3 (2023).

[33] N. Morales-Durán, J. Wang, G. R. Schleder, M. Angeli, Z. Zhu, E. Kaxiras, C. Repellin, and J. Cano, *Pressure-Enhanced Fractional Chern Insulators in Moiré Transition Metal Dichalcogenides along a Magic Line*, Phys. Rev. Res. **5**, L032022 (2023).

[34] A. P. Reddy, F. F. Alsallom, Y. Zhang, T. Devakul, and L. Fu, *Fractional Quantum Anomalous Hall States in Twisted Bilayer* $MoTe_2$ *and* $WSe_2$, Phys. Rev. B **108**, 085117 (2023).

[35] C. Wang *et al.*, *Fractional Chern Insulator in Twisted Bilayer* $MoTe_2$, arXiv:2304.11864.

[36] N. Morales-Durán, N. Wei, and A. H. MacDonald, *Magic Angles and Fractional Chern Insulators in Twisted Homobilayer TMDs*, arXiv:2308.03143.

[37] P. Mai, J. Zhao, B. E. Feldman, and P. Phillips, $1/4$ *Is the New* $1/2$*: Interaction-Induced Unification of Quantum Anomalous and Spin Hall Effects*, arXiv:2210.11486.

[38] B. A. Foutty *et al.*, *Mapping Twist-Tuned Multi-Band Topology in Bilayer* $WSe_2$, arXiv:2304.09808.

[39] F. Wu, T. Lovorn, E. Tutuc, and A. H. MacDonald, *Hubbard Model Physics in Transition Metal Dichalcogenide Moiré Bands*, Phys. Rev. Lett. **121**, 026402 (2018).

[40] E. C. Regan *et al.*, *Mott and Generalized Wigner Crystal States in* $WSe_2/WS_2$ *Moiré Superlattices*, Nature (London) **579**, 359 (2020).

[41] Y. Tang *et al.*, *Simulation of Hubbard Model Physics in* $WSe_2/WS_2$ *Moiré Superlattices*, Nature (London) **579**, 353 (2020).

[42] Y. Xu, S. Liu, D. A. Rhodes, K. Watanabe, T. Taniguchi, J. Hone, V. Elser, K. F. Mak, and J. Shan, *Correlated Insulating States at Fractional Fillings of Moiré Superlattices*, Nature (London) **587**, 214 (2020).

[43] Z. Chu *et al.*, *Nanoscale Conductivity Imaging of Correlated Electronic States in* $WSe_2/WS_2$ *Moiré Superlattices*, Phys. Rev. Lett. **125**, 186803 (2020).

[44] X. Huang *et al.*, *Correlated Insulating States at Fractional Fillings of the* $WS_2/WSe_2$ *Moiré Lattice*, Nat. Phys. **17**, 715 (2021).

[45] C. Jin *et al.*, *Stripe Phases in* $WSe_2/WS_2$ *Moiré Superlattices*, Nat. Mater. **20**, 940 (2021).

[46] T. Li, J. Zhu, Y. Tang, K. Watanabe, T. Taniguchi, V. Elser, J. Shan, and K. F. Mak, *Charge-Order-Enhanced Capacitance in Semiconductor Moiré Superlattices*, Nat. Nanotechnol. **16**, 1068 (2021).

[47] E. Liu, T. Taniguchi, K. Watanabe, N. M. Gabor, Y.-T. Cui, and C. H. Lui, *Excitonic and Valley-Polarization Signatures of Fractional Correlated Electronic Phases in a* $WSe_2/WS_2$ *Moiré Superlattices*, Phys. Rev. Lett. **127**, 037402 (2021).

[48] See Supplemental Material at http://link.aps.org/supplemental/10.1103/PhysRevX.13.031037 for data of

device II, calculation results, and more supplemental data.

[49] C. Xu *et al.*, *Maximally Localized Wannier Orbitals, Interaction Models and Fractional Quantum Anomalous Hall Effect in Twisted Bilayer* $MoTe_2$, arXiv:2308.09697.

[50] H. Park *et al.*, *Observation of Fractionally Quantized Anomalous Hall Effect*, Nature (London), 10.1038/s41586-023-06536-0 (2023).

[51] L. Wang *et al.*, *One-Dimensional Electrical Contact to a Two-Dimensional Material*, Science **342**, 614 (2013).

[52] T. Li *et al.*, *Continuous Mott Transition in Semiconductor Moiré Superlattices*, Nature (London) **597**, 350 (2021).